

Redox-Active Metaphosphate-Like Terminals Enable High-Capacity MXene Anodes for Ultrafast Na-Ion Storage


Boya Sun, Qiongqiong Lu, Kaixuan Chen, Wenhao Zheng, Zhongquan Liao, Nikolaj Lopatik, Dongqi Li, Martin Hantusch, Shengqiang Zhou, Hai I. Wang, Zdeněk Sofer, Eike Brunner, Ehrenfried Zschech, Mischa Bonn, Richard Dronskowski, Daria Mikhailova, Qinglei Liu,* Di Zhang, Minghao Yu,* and Xinliang Feng*

2D transition metal carbides and/or nitrides, so-called MXenes, are noted as ideal fast-charging cation-intercalation electrode materials, which nevertheless suffer from limited specific capacities. Herein, it is reported that constructing redox-active phosphorus–oxygen terminals can be an attractive strategy for Nb₄C₃ MXenes to remarkably boost their specific capacities for ultrafast Na⁺ storage. As revealed, redox-active terminals with a stoichiometric formula of PO₂⁻ display a metaphosphate-like configuration with each P atom sustaining three P–O bonds and one P=O dangling bond. Compared with conventional O-terminals, metaphosphate-like terminals empower Nb₄C₃ (denoted PO₂-Nb₄C₃) with considerably enriched carrier density (four-fold), improved conductivity (12.3-fold at 300 K), additional redox-active sites, boosted Nb redox depth, nondeclined Na⁺-diffusion capability, and buffered internal stress during Na⁺ intercalation/de-intercalation. Consequently, compared with O-terminated Nb₄C₃, PO₂-Nb₄C₃ exhibits a doubled Na⁺-storage capacity (221.0 mAh g⁻¹), well-retained fast-charging capability (4.9 min at 80% capacity retention), significantly promoted cycle life (nondegraded capacity over 2000 cycles), and justified feasibility for assembling energy–power-balanced Na-ion capacitors. This study unveils that the molecular-level design of MXene terminals provides opportunities for developing simultaneously high-capacity and fast-charging electrodes, alleviating the energy–power tradeoff typical for energy-storage devices.

1. Introduction

The exponential growth of the sustainable energy market is pushing the development of economically feasible energy-storage technologies at all scales.^[1] Adopting resource-abundant Na⁺ charge carriers to replace scarce Li⁺ (23 000 ppm vs 20 ppm in the earth's crust) of state-of-the-art lithium-ion batteries is promising to bring down the manufacturing cost and thus promote the affordability of electrochemical energy-storage devices.^[2] Nevertheless, the energy–power tradeoff issue commonly seen in Li⁺ systems becomes even more severe for Na⁺ systems, which originates from the larger ionic size (1.02 Å vs 0.76 Å for sixfold coordination), heavier relative atomic mass (23 vs 7), and higher redox potential (−2.71 V vs −3.05 V in relation to the standard hydrogen electrode) of Na⁺ compared with Li⁺.^[3] In this sense, it is crucial to rationally reconstruct the established Li⁺-storage electrode materials to fit into the smooth Na⁺ accommodation with simultaneously fast-charging and high-capacity behavior.

B. Sun, Q. Liu, D. Zhang
State Key Laboratory of Metal Matrix Composites
School of Materials Science and Engineering
Shanghai Jiao Tong University
Shanghai 200240, China
E-mail: liuqinglei@sjtu.edu.cn

 The ORCID identification number(s) for the author(s) of this article can be found under <https://doi.org/10.1002/adma.202108682>.

© 2022 The Authors. Advanced Materials published by Wiley-VCH GmbH. This is an open access article under the terms of the Creative Commons Attribution-NonCommercial-NoDerivs License, which permits use and distribution in any medium, provided the original work is properly cited, the use is non-commercial and no modifications or adaptations are made.

DOI: 10.1002/adma.202108682

B. Sun, D. Li, M. Yu, X. Feng
Faculty of Chemistry and Food Chemistry & Center for Advancing Electronics Dresden (cfaed)
Technische Universität Dresden
01062 Dresden, Germany
E-mail: minghao.yu@tu-dresden.de; xinliang.feng@tu-dresden.de

Q. Lu, M. Hantusch, D. Mikhailova
Leibniz Institute for Solid State and Materials Research (IFW)
Dresden e.V.
01069 Dresden, Germany

K. Chen, R. Dronskowski
Chair of Solid-State and Quantum Chemistry
Institute of Inorganic Chemistry
RWTH Aachen University
D-52056 Aachen, Germany

W. Zheng, H. I. Wang, M. Bonn
Max Planck Institute for Polymer Research
Ackermannweg 10, D-55128 Mainz, Germany

MXenes, sharing a formula $M_{n+1}X_nT_x$ ($n = 1-4$, M is a transition metal, X refers to carbon and/or nitrogen, T_x represents terminals), have captured widespread attention as a group of multifunctional 2D materials.^[4] Notably, the fast-charging capability of MXenes as energy-storage electrodes has been widely exemplified for accommodating diverse cations, including large-sized Na ions.^[5] Such attractive fast-charging capability benefits from the combination of the large slit-shaped 2D nanochannels and high electrical conductivity (up to $11\,000\text{ S cm}^{-1}$),^[6] ensuring MXenes with simultaneous rapid ion and charge transport. However, the bottleneck of MXenes for energy storage has also clearly been identified, that is, the low specific capacity (generally less than 150 mAh g^{-1} for Na^+ storage).^[7] Intrinsically, the low specific capacities of MXenes are associated with the pseudocapacitive charge-storage mechanism, in which the intercalated cation interacting with surface terminals of MXenes induce only slight redox depth of the metal elements.^[7a,8]

Early studies have vividly revealed that terminals of MXenes played a crucial role in determining the charge-storage behavior of MXenes. This is because terminals define the surface chemistries of MXenes and affect the affinity with the intercalated cations.^[9] For example, density functional theory (DFT) calculations suggested that, among conventional terminals of MXenes (i.e., O-, OH-, F-terminals), O-terminals contributed to the highest Li^+ -storage capacity.^[10] Meanwhile, the strongly electronegative OH-terminals led to irreversible Li^+ storage, and F-terminals deteriorated the conductivity.^[11] The theoretical result was also verified by a recent experimental effort, in which Cl-/O-terminated Ti_3C_2 MXene without OH- and F-terminals (produced via a molten salt method) was shown to possess higher Li^+ -storage capacity than the HF-etched Ti_3C_2 MXene.^[12] Despite the achieved understanding, straightforward terminal regulation approaches for directly enhancing the specific capacity of MXene have seldom been realized.

This work provides such a surface regulation method, where redox-active metaphosphate-like terminals with a stoichiometric

formula of PO_2^- are disclosed to greatly boost the specific capacity of MXenes for Na^+ storage. Here, Nb_4C_3 MXene with metaphosphate-like terminals (denoted $\text{PO}_2\text{-Nb}_4\text{C}_3$) is constructed via a targeted terminal conversion approach by annealing the hybrid membrane consisting of $\text{Nb}_4\text{C}_3\text{T}_x$ MXene and black phosphorus (BP). Compared with conventional O-terminated Nb_4C_3 (denoted O- Nb_4C_3 , 96.5 mAh g^{-1}), $\text{PO}_2\text{-Nb}_4\text{C}_3$ displays a doubled Na^+ -storage capacity (221.0 mAh g^{-1}), surpassing most reported MXenes for Na^+ storage. The additional redox sites and enhanced redox depth of Nb induced by PO_2^- terminals are uncovered to be responsible for the capacity improvement. Impressively, the high specific capacity of $\text{PO}_2\text{-Nb}_4\text{C}_3$ comes without sacrificing the fast-charging capability, which can be assigned to a fourfold enriched carrier density, increased conductivity (by a factor of 12.3 at 300 K), and nondeclined Na^+ -diffusion capability. Short charging times of 4.9 min and 20.4 s are achieved by the $\text{PO}_2\text{-Nb}_4\text{C}_3$ electrode at capacity retention of 80% and 51%, respectively. Moreover, PO_2^- terminals are demonstrated to buffer the internal stress of Nb_4C_3 during Na^+ intercalation/de-intercalation, contributing to the improved cycling life (nondegraded capacity over 2000 cycles). Paired with N-doped hierarchical porous carbon (NHPC) cathodes, the $\text{PO}_2\text{-Nb}_4\text{C}_3$ electrodes are further used to assemble Na-ion capacitor devices, which deliver the maximum energy density of 55 Wh L^{-1} and supercapacitor-level power density (9765 W L^{-1}). Our redox-active terminal design for MXenes satisfies the stringent requirement for constructing energy-power-balanced energy-storage devices.

2. Results

2.1. Synthesis and Characterization of $\text{PO}_2\text{-Nb}_4\text{C}_3$

Nb_4C_3 MXene, as a typical M_4X_3 MXene, was selected as the research object in this study for its better chemical stability than M_3X_2 and M_2X MXenes according to the recent simulation effort.^[13] Also, Nb_4C_3 MXene has been proved with excellent conductivity^[14] and large interlayer spacing, enabling it with considerably better cycling and rate performance than other MXene materials for lithium-ion batteries.^[15] The synthetic route of $\text{PO}_2\text{-Nb}_4\text{C}_3$, relying on a targeted terminal conversion approach, is illustrated in **Figure 1a**. Initially, $\text{Nb}_4\text{C}_3\text{T}_x$ MXene nanoflakes were prepared through a conventional HF-etching and delamination method (Figure S1, Supporting Information), while BP nanoflakes were delaminated from bulk BP via a facile electrochemical method developed by our group (Figure S2, Supporting Information).^[16] Zeta potential measurements indicate that both $\text{Nb}_4\text{C}_3\text{T}_x$ and BP nanoflakes are featured by negative surface charges. To promote the self-assembly of $\text{Nb}_4\text{C}_3\text{T}_x$ and BP through the electrostatic interaction, the cationic surfactant cetyltrimethylammonium bromide (CTAB), was subsequently grafted onto BP nanoflakes to turn the surface positively charged (Figure S3, Supporting Information). Electrodes constructed by horizontally stacked nanosheets are generally considered unfavorable for the fast ion transport due to the long ion transport pathways and poor electrolyte penetration into the electrode, which further results in the unsatisfying fast-charging capability of the electrode.^[17] Introducing

Z. Liao
Fraunhofer Institute for Ceramic Technologies and Systems (IKTS)
Maria-Reiche-Strasse 2, 01109 Dresden, Germany

N. Lopatik, E. Brunner
Chair of Bioanalytical Chemistry
Faculty of Chemistry and Food Chemistry
Technische Universität Dresden
01062 Dresden, Germany

S. Zhou
Institute of Ion Beam Physics and Materials Research
Helmholtz-Zentrum Dresden-Rossendorf
01328 Dresden, Germany

Z. Sofer
Department of Inorganic Chemistry
University of Chemistry and Technology Prague
Technická 5, Prague 6, 166 28, Czech Republic

E. Zschech
Faculty of Chemistry
University of Warsaw
ul. Żwirki i Wigury 101, Warsaw 02-089, Poland

X. Feng
Max Planck Institute of Microstructure Physics
Weinberg 2, 06120 Halle, Germany

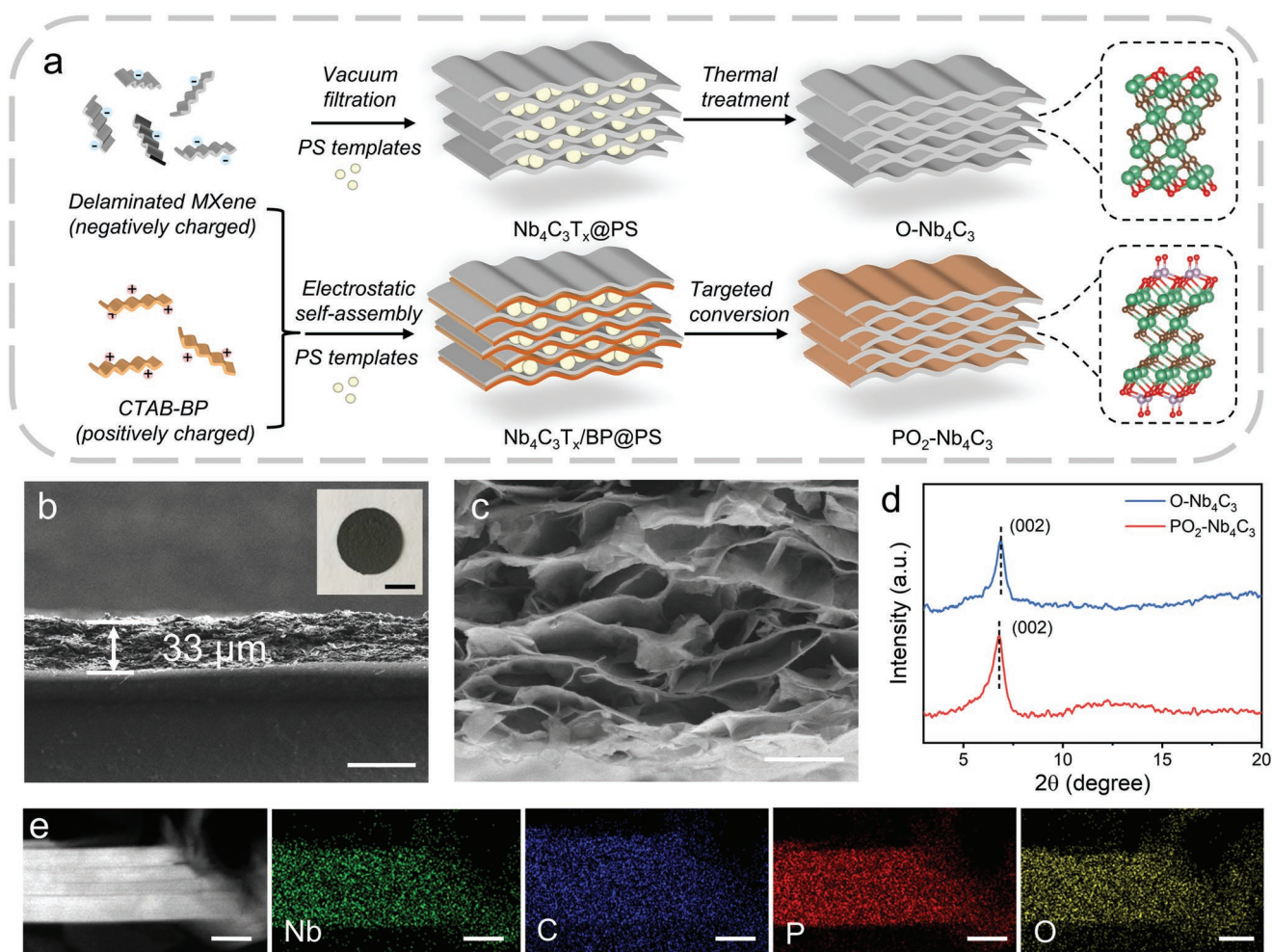


Figure 1. a) Schematic illustration of the fabrication routes for O-Nb₄C₃ and PO₂-Nb₄C₃. b, c) Cross-sectional SEM images of the PO₂-Nb₄C₃ film, with the inset of (b) showing a digital photo of the freestanding film. d) XRD patterns of O-Nb₄C₃ and PO₂-Nb₄C₃. e) HAADF-STEM image of the PO₂-Nb₄C₃ film and corresponding EDX mappings for Nb, C, P, and O. Scale bars: (b) 50 μm, inset image of (b) 1 cm, (c) 1 μm, (e) 20 nm.

interconnected channels within horizontally stacked nanosheets represents an efficient way to improve the electrolyte penetration into the electrode and shorten the ion transport pathways.^[8] In this regard, polystyrene (PS) microspheres were used as templates to construct the 3D interconnected structure for the PO₂-Nb₄C₃ electrode, which can simultaneously prevent the restacking of nanosheets and improve the ion accessibility to redox-active sites. Specifically, the Nb₄C₃T_x dispersion, CTAB-BP dispersion, and PS microsphere templates (400 nm in diameter, Figure S4, Supporting Information) were mixed, sonicated, and vacuum-filtrated into the freestanding film (denoted Nb₄C₃T_x/BP@PS). Finally, the PO₂-Nb₄C₃ film (33 μm in thickness, Figure 1b) was obtained by annealing Nb₄C₃T_x/BP@PS at 500 °C in Ar gas for 1 h. Importantly, to guarantee the similar surface area of Nb₄C₃T_x and BP, a mass ratio of 3.24 between Nb₄C₃T_x and BP was controlled for the layer-by-layer assembly (Figures S5 and S6, Supporting Information). During annealing, the PS templates were removed to empower the PO₂-Nb₄C₃ film with a 3D open structure (Figure 1c and Figure S6, Supporting Information). Meanwhile, the terminals of Nb₄C₃T_x were converted into PO₂⁻ by decomposing BP. For

comparison, the O-Nb₄C₃ film was also fabricated by a similar method without adding CTAB-BP (Figure S7, Supporting Information).

X-ray diffraction (XRD) uncovers the similar crystal-line structures of O-Nb₄C₃ and PO₂-Nb₄C₃ (Figure 1d and Figure S8, Supporting Information). The close (002) peak positions of O-Nb₄C₃ and PO₂-Nb₄C₃ imply that PO₂-terminals only slightly enlarge the interlayer distance of Nb₄C₃ (1.33 nm) in comparison with O-Nb₄C₃ (1.29 nm). This result is consistent with the high-resolution transmission electron microscopy (TEM) images of O-Nb₄C₃ (Figure S9, Supporting Information) and PO₂-Nb₄C₃ (Figure S10, Supporting Information). High-angle annular dark-field scanning transmission electron microscopy (HAADF-STEM) coupled with energy-dispersive X-ray analysis (EDX) reveals the uniform distribution of Nb, C, P, and O in PO₂-Nb₄C₃ (Figure 1e). As no impurity phase was observed in the selected-area electron diffraction (SAED) pattern (Figure S11, Supporting Information) of PO₂-Nb₄C₃, we can conclude that P exists on the surface Nb₄C₃ as part of the terminals. The atomic ratio of Nb/P/O elements in PO₂-Nb₄C₃ is quantitatively confirmed to be 2:1.03:2.17 (Figure S10,

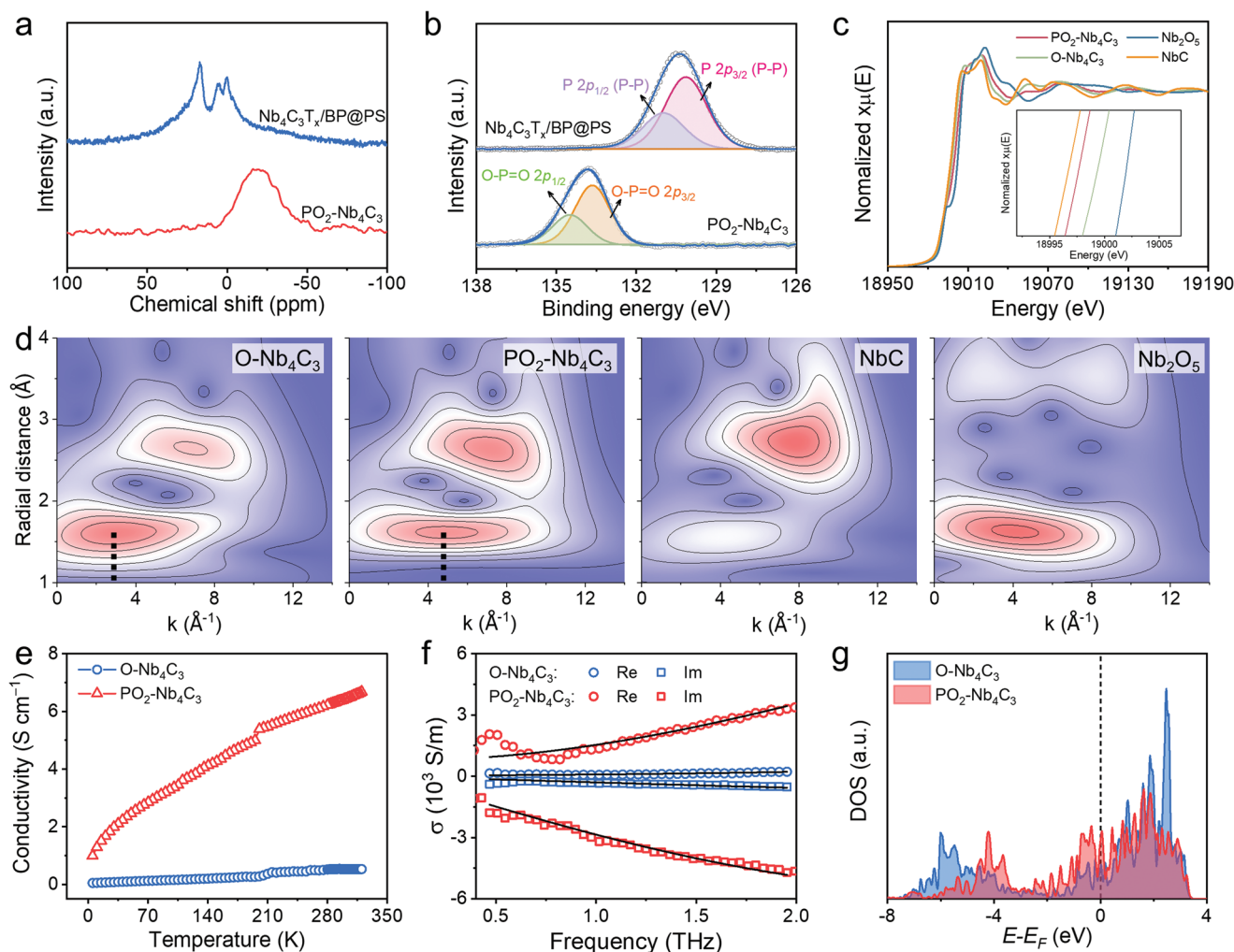


Figure 2. a) Solid-state ^{31}P NMR and b) high-resolution P 2p XPS spectra of $\text{Nb}_4\text{C}_3\text{T}_x/\text{BP}@PS$ and $\text{PO}_2\text{-Nb}_4\text{C}_3$. c) The normalized Nb K-edge XAS and d) the contour plots of the wavelet-transformed EXAFS of $\text{O-Nb}_4\text{C}_3$, $\text{PO}_2\text{-Nb}_4\text{C}_3$, and standard references. e) Electrical conductivities of $\text{O-Nb}_4\text{C}_3$ and $\text{PO}_2\text{-Nb}_4\text{C}_3$ measured by the van der Pauw method. f) Frequency-resolved THz conductivity of $\text{O-Nb}_4\text{C}_3$ and $\text{PO}_2\text{-Nb}_4\text{C}_3$ samples, and the solid lines show the fitting result of Drude–Smith model. g) The projected DOS of outer Nb site in $\text{O-Nb}_4\text{C}_3$ and $\text{PO}_2\text{-Nb}_4\text{C}_3$.

Supporting Information). By contrast, $\text{O-Nb}_4\text{C}_3$ shows the presence of only Nb, C, and O (Figure S8, Supporting Information). No F was detected for both $\text{O-Nb}_4\text{C}_3$ and $\text{PO}_2\text{-Nb}_4\text{C}_3$ (Figure S12, Supporting Information), which agrees well with a previous report that revealed the removal of F- and OH-terminals of MXenes during annealing.^[11b] Notably, the removal of F- and OH-terminals is desirable for MXenes used in batteries, as early studies verified that F- and OH-terminals decreased the electronic conductivity and brought the irreversible capacity.^[11,18]

Solid-state ^{31}P magic-angle spinning (MAS) nuclear magnetic resonance (NMR) studies were conducted to further elucidate the PO_2 -terminal configuration and the structural evolution of Nb_4C_3 . As revealed by Figure 2a, $\text{Nb}_4\text{C}_3\text{T}_x/\text{BP}@PS$ and $\text{PO}_2\text{-Nb}_4\text{C}_3$ exhibit quite distinguished ^{31}P MAS NMR spectra. In agreement with the earlier reported studies on BP,^[19] $\text{Nb}_4\text{C}_3\text{T}_x/\text{BP}@PS$ displays characteristic peaks of P–P bonds and oxidized P species like P–O and O–P=O (Figure S13, Supporting Information). After annealing, $\text{PO}_2\text{-Nb}_4\text{C}_3$ displays a broad signal centered at about -19 ppm. The absence

of the above-described characteristic signals for BP reveals the complete conversion of BP in $\text{PO}_2\text{-Nb}_4\text{C}_3$. Besides, the chemical shift in the region around -19 ppm is typical for metaphosphates (e.g., cyclic trimetaphosphate^[20]), suggesting that the local coordination environment of terminal P shows a metaphosphate-like configuration with three P–O bonds and one P=O bond.

The same conclusion can be drawn by the P 2p X-ray photoelectron spectroscopy (XPS) analysis (Figure 2b). No BP characteristic peaks (P–P $2p_{3/2}$ and $2p_{1/2}$ peaks at 130.2 and 131.0 eV) were detected for $\text{PO}_2\text{-Nb}_4\text{C}_3$. Instead, the P 2p peak of $\text{PO}_2\text{-Nb}_4\text{C}_3$ displays a considerably higher binding energy, being deconvoluted into O–P=O $2p_{3/2}$ (133.6 eV) and $2p_{1/2}$ (134.5 eV) peaks. These peaks agree well with the feature of metaphosphate^[21] and pyrophosphate.^[22] A consistent result is also identified in the Fourier transform infrared (FTIR) spectrum of $\text{PO}_2\text{-Nb}_4\text{C}_3$ (Figure S14, Supporting Information), which displays apparent peaks associated with P–O bonds (stretching vibration at 1043 and 1085 cm^{-1}) and dangling P=O

bonds (symmetric stretching vibration at 1174 cm⁻¹).^[19] Besides, Nb–O–P and P=O bonds were also identified in the O 1s spectrum of PO₂-Nb₄C₃, which significantly contrasts with the O 1s spectrum of O-Nb₄C₃ consisting of only C–Nb–O_x (Figure S15, Supporting Information). The quantitative analysis of XPS spectra reveals that the Nb/P/O atomic ratio in PO₂-Nb₄C₃ is 2:1.08:2.15, which agrees well with the EDX mapping result. Given above characterizations, the terminal conversion reactions are assumed to include the following steps: 1) OH- and F-terminals are dissociated from the MXene surface during the thermal annealing, which was previously documented for other MXenes.^[11,23] 2) The thermally decomposed BP atoms react with the remaining O-terminals on Nb₄C₃ MXene, dissociated OH-terminals, and the original surface O atoms on BP to form PO_x anionic species attached on the surface of Nb₄C₃ MXene. 3) Upon the exposure to ambient environment, the formed PO_x-terminals could be further oxidized by the air and form the stable PO₂-terminals.

Furthermore, Nb K-edge X-ray absorption spectra (XAS) of O-Nb₄C₃ and PO₂-Nb₄C₃ were measured to clarify the local coordination environment change of Nb atoms induced by different terminals. As revealed in Figure 2c, the edge energy of PO₂-Nb₄C₃ (19 000.9 eV) is less than that of O-Nb₄C₃ (19 001.4 eV), suggesting a lower valence state of Nb in PO₂-Nb₄C₃ than that in O-Nb₄C₃. By establishing the linear relationship between the K-edge energy and Nb valence with NbC and Nb₂O₅ references, the average valences of Nb are determined to be 4.18 in PO₂-Nb₄C₃ and 4.31 in O-Nb₄C₃ (Figure S16a, Supporting Information). The wavelet-transform analysis with a 2D representation of the extended X-ray absorption fine structure (EXAFS) spectra in *R* and *k* spaces clearly uncovers the local coordination conditions of Nb in O-Nb₄C₃ and PO₂-Nb₄C₃ (Figure 2d). For the contour intensity, there are two maximum values corresponding to the Fourier-transform EXAFS peaks at 1.6 and 2.8 Å in *R* space (Figure S16b, Supporting Information). The former peak can be attributed to the Nb–C(O) scattering, while the latter matches well with the Nb–C–Nb scattering. Compared with O-Nb₄C₃ (centered at 3.0 Å⁻¹), PO₂-Nb₄C₃ (centered at 4.8 Å⁻¹) presents an obvious positive shift of the Nb–C(O) peak in *k* space, which is indicative of the Nb–C(O) bond length increase. The bond length change induced by PO₂-terminals can also be reflected by the position differences of characteristic Nb–C and Nb–O Raman peaks between O-Nb₄C₃ and PO₂-Nb₄C₃ (Figure S17, Supporting Information). Based on the above qualitative and quantitative analysis of the terminal configuration, we have further conducted density-functional theory (DFT) simulation for O-Nb₄C₃ and PO₂-Nb₄C₃ to specify the bond change trend (see details in Figure S18, Supporting Information). As revealed, the Nb–O bond, referring to the connection between Nb₄C₃ and terminals, shows a much larger length in PO₂-Nb₄C₃ (2.61 Å) than in O-Nb₄C₃ (2.11 Å).

2.2. Electrical Transport Properties

Next, we evaluate how PO₂-terminals, in comparison with O-terminals, affect the electrical transport properties of Nb₄C₃ films. Using the van der Pauw four-probe method (Figure 2e and Figure S19, Supporting Information), the conductivity of

the PO₂-Nb₄C₃ film (6.41 S cm⁻¹) was verified to be about one order of magnitude (roughly 13 times) higher than that of the O-Nb₄C₃ film (0.52 S cm⁻¹) at 300 K.

To investigate the origin of the conductivity enhancement, we investigated complementarily the conductivity of samples by terahertz time-domain spectroscopy (THz-TDS).^[24] In the study, we probe the intrinsic conductivity of the sample by a single cycle THz with a bandwidth up to ≈2 THz. The time-domain THz electrical field, with and without the MXene samples, can be mapped out and converted into frequency-resolved THz conductivity ($\sigma(\omega)$) (Figure 2f).^[24] As discovered, PO₂-Nb₄C₃ was shown to have an order of magnitude higher conductivity than O-Nb₄C₃. This result is perfectly in line with the electrical transport data measured by the van der Pauw method. Note that, the conductivity (σ) is proportional to the charge carrier density (*N*) and carrier momentum scattering time (τ). To disentangle the contribution of *N* from τ to the conductivity, we applied Drude–Smith model to describe the charge transport properties of MXenes [as expressed in Equation (1) with *m*^{*} the effective mass of charge carriers].^[25] Different from the standard Drude model with isotropic momentum scattering process, a parameter *c* is implemented in the Drude–Smith model to characterize an anisotropic charge backscattering effect, with the values ranging from 0 (isotropic scattering, Drude-like transport) to –1 (completely backscattering). As indicated in Figure 2f, the Drude–Smith model can fit our results well, and the inferred charge transport parameters, including τ and *c*, are listed in Table S1 (Supporting Information). Accordingly, we can conclude that the enhanced conductivity in PO₂-Nb₄C₃ versus O-Nb₄C₃ originates from a combination of higher carrier density (increased fourfold), longer charge scattering time (21 ± 1 fs vs 12 ± 2 fs), and slightly weaker backscattering effect (–0.97 vs –0.99), with carrier density as the dominant factor

$$\sigma(\omega) = \frac{N\tau e^2}{m^*(1-i\omega\tau)} \left(1 + \frac{c}{1-i\omega\tau} \right) \quad (1)$$

Moreover, the simulated band structures of O-Nb₄C₃ and PO₂-Nb₄C₃ are displayed in Figure S18 (Supporting Information). The projected density of states (DOS) of O-Nb₄C₃ and PO₂-Nb₄C₃ (Figure S20, Supporting Information) reveal that the electronic states in the vicinity of the Fermi level are dominated by the Nb d band, which results from the overlapping of the filled lower Hubbard band (denoted LHB) and empty upper Hubbard bands (denoted UHB). Compared with O-terminals, PO₂-terminals remarkably enhance the metallic d electronic states from the outer-shell Nb atoms (i.e., terminal-connected Nb atoms, Figure 2g), thus contributing to the boosted conductivity of PO₂-Nb₄C₃. The calculations are therefore perfectly in line with both the electrical and THz results. All these superior electrical properties are beneficial for PO₂-Nb₄C₃ to retain the fast-charging capability.

2.3. Considerable Enhancement of Na⁺-Storage Capacity

The Na⁺-storage capability of the free-standing and binder-free O-Nb₄C₃ and PO₂-Nb₄C₃ films (loading mass of about 2 mg cm⁻²) were directly assessed in an electrolyte of

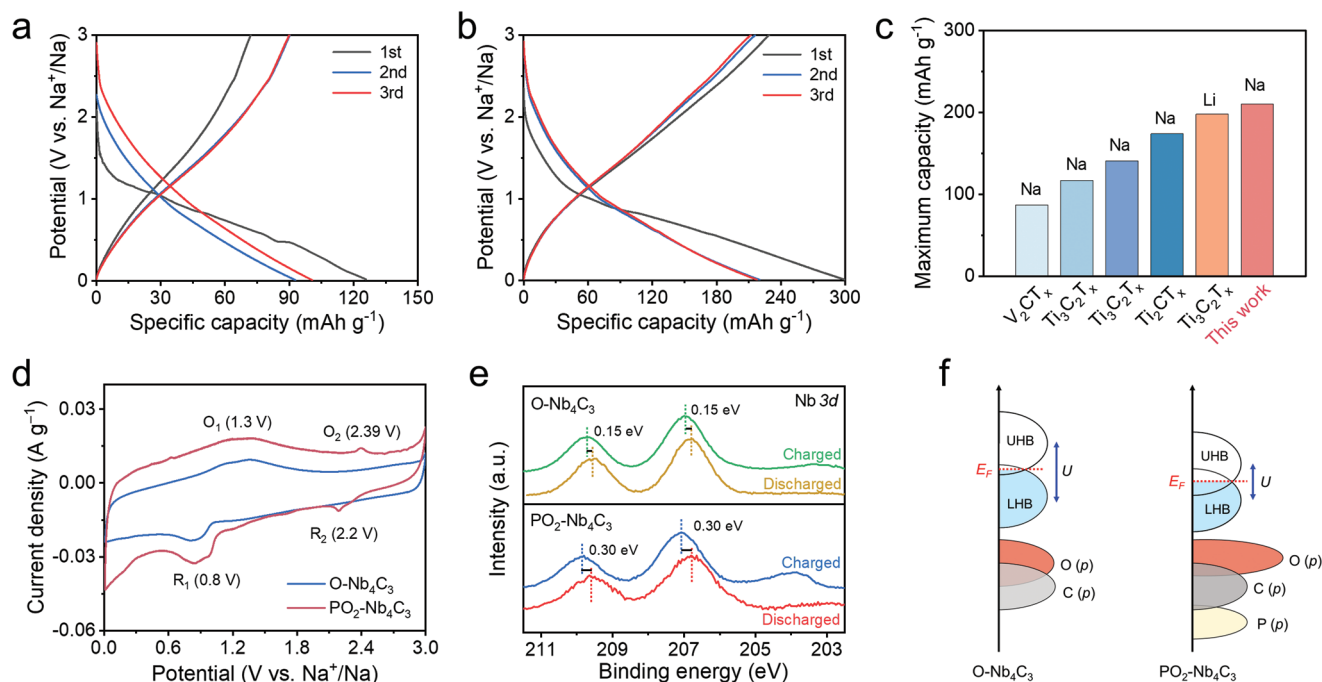


Figure 3. Na⁺-storage capacity. a,b) The initial three GCD curves of the O-Nb₄C₃ (a) and PO₂-Nb₄C₃ (b) electrodes at 0.05 A g⁻¹. c) The maximum specific capacity of PO₂-Nb₄C₃ in comparison with those of reported MXenes for Li⁺ and Na⁺ storage. d) CV curves of the O-Nb₄C₃ and PO₂-Nb₄C₃ electrodes at 0.1 mV s⁻¹. e) Nb 3d XPS spectra of the O-Nb₄C₃ and PO₂-Nb₄C₃ electrodes at the fully discharged and charged stages. f) Schematic energy bands of O-Nb₄C₃ and PO₂-Nb₄C₃ in consideration of Mott–Hubbard splitting.

1.0 M NaPF₆ dissolved in diethylene glycol dimethyl ether (DEGDME). **Figure 3a,b** compares the first three galvanostatic charge/discharge (GCD) cycles of the O-Nb₄C₃ and PO₂-Nb₄C₃ electrodes at 0.05 A g⁻¹. In the first cycle, the PO₂-Nb₄C₃ electrode depicts a substantially higher Coulombic efficiency of 78% than the O-Nb₄C₃ electrode (57%). Impressively, the PO₂-Nb₄C₃ electrode delivers an excellent reversible specific capacity of 221.0 mAh g⁻¹, more than twice the specific capacity of the O-Nb₄C₃ electrode (96.5 mAh g⁻¹). Moreover, the Na⁺-storage capacity of PO₂-Nb₄C₃ is superior to the most recently reported Na⁺-storage MXenes (Figure 3c),^[7] and even surpasses the Li⁺-storage capacity of the microporous Ti₃C₂ electrode (145 mAh g⁻¹).^[12a]

The additional redox reaction brought by redox-active PO₂-terminals is essential for the greatly enhanced Na⁺-storage capacity of PO₂-Nb₄C₃. The calculated electron localization functions (ELFs, Figure S21, Supporting Information) show a uniform floating electron gas above the oxygen atoms and PO₂-terminals. Particularly, O atoms are suggested as Na⁺ adsorption centers, as they give rise to apparent nucleophilic features with dense electrons. As straightforward evidence, the cyclic voltammetry (CV) curve of the PO₂-Nb₄C₃ electrode presents an apparent pair of redox peaks (R₂/O₂) at 2.2/2.39 V versus Na⁺/Na, which is not observed for the O-Nb₄C₃ electrode. These redox peaks are suggested to be associated with PO₂-terminals by the P 2p XPS spectra of PO₂-Nb₄C₃ at fully charged/discharged stages (Figure S22, Supporting Information). At the discharged stage (0.01 V vs Na⁺/Na), the P 2p XPS peak of PO₂-Nb₄C₃ shows an apparent shift towards the lower binding energy, indicating the formation of electron-deficient P due to

the Na⁺ adsorption. Thus, redox reactions of PO₂-terminals during the discharge and charge processes can result in additional capacity.

Besides, the Nb 3d XPS spectra indicate that PO₂-terminals could induce the higher redox depth of Nb in Nb₄C₃ than O-terminals, which also contributes to the capacity enhancement of the PO₂-Nb₄C₃ electrode. The Nb 3d XPS spectrum of PO₂-Nb₄C₃ presents a larger shift (0.30 eV) than O-Nb₄C₃ (0.15 eV) during the discharge/charge process, which manifests the deeper redox depth of Nb in PO₂-Nb₄C₃ (Figure 3e). By revisiting the simulated DOS results of O-Nb₄C₃ and PO₂-Nb₄C₃ (Figure S20, Supporting Information), one can notice that PO₂-terminals shift the metallic Nb d band to a lower energy range, accompanied by the enhanced overlapping of LHB and UHB (Figure 3f). Such a band structure promotes the electron jumping between the occupied and unoccupied metallic bands, thus probably accounting for the higher Nb redox depth of PO₂-Nb₄C₃. Overall, the capacity improvement of PO₂-Nb₄C₃ can be assigned to PO₂-terminals, which provide additional redox-active sites and enhance the redox depth of Nb.

2.4. Fast-Charging Capability

The tradeoff between the specific capacity and rate capability is commonly observed for ion-intercalation electrodes, because high-depth redox reactions always suffer from the kinetics issue associated with charge/ion transport.^[26] In this regard, we like to highlight that the capacity enhancement of PO₂-Nb₄C₃ comes without sacrificing the fast-charging capability.

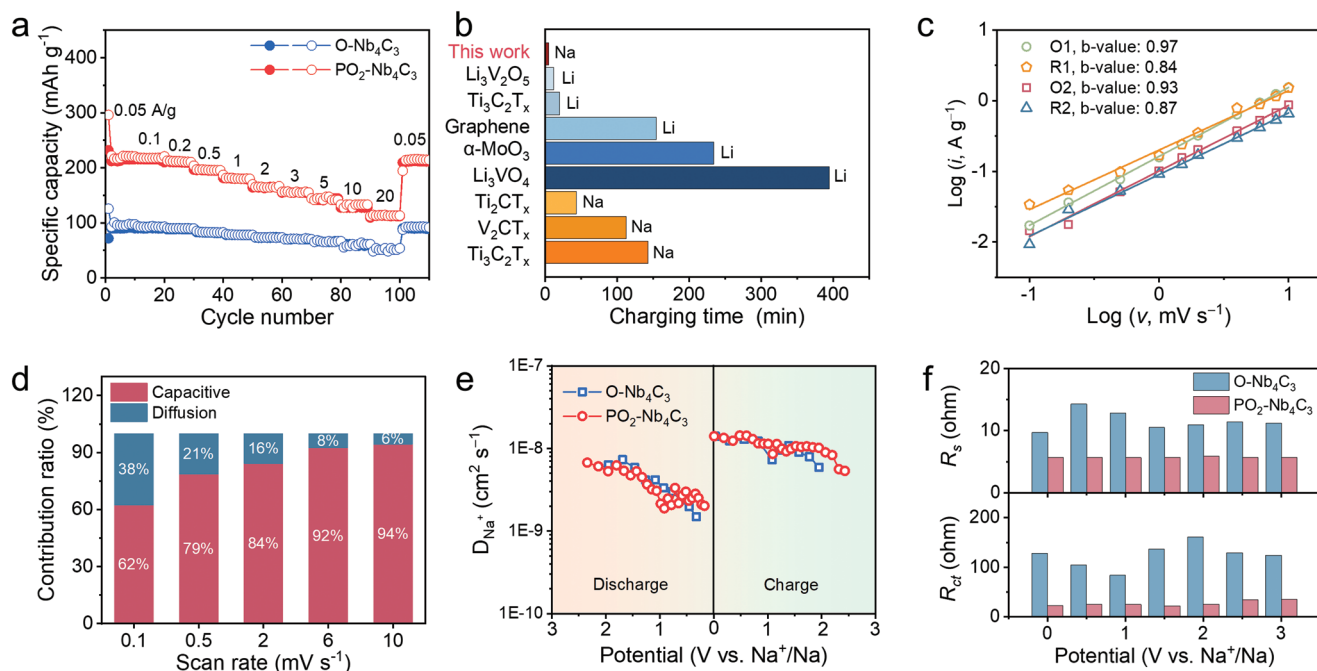


Figure 4. Fast-charging capability of the $\text{PO}_2\text{-Nb}_4\text{C}_3$ electrode. a) Rate performance of the $\text{O-Nb}_4\text{C}_3$ and $\text{PO}_2\text{-Nb}_4\text{C}_3$ electrodes at various current densities from 0.05 to 20 A g^{-1} . b) Charging times at 80% capacity retention of the $\text{PO}_2\text{-Nb}_4\text{C}_3$ electrode and reported high-rate electrodes.^[7a–d,12a,26a] c) $\text{Log}(i)$ versus $\text{log}(v)$ for the redox peaks of the $\text{PO}_2\text{-Nb}_4\text{C}_3$ electrode. d) Capacitive contribution and diffusion contribution of the $\text{PO}_2\text{-Nb}_4\text{C}_3$ electrode at different scan rates. e) Na^+ diffusion coefficients of the $\text{O-Nb}_4\text{C}_3$ and $\text{PO}_2\text{-Nb}_4\text{C}_3$ electrodes calculated from the GITT measurements. f) R_s and R_{ct} of the $\text{O-Nb}_4\text{C}_3$ and $\text{PO}_2\text{-Nb}_4\text{C}_3$ electrodes at different potentials.

When the current density increases to 20 A g^{-1} (charging time of 20.4 s), $\text{PO}_2\text{-Nb}_4\text{C}_3$ can still maintain a specific capacity of 113.6 mAh g^{-1} , reflecting high capacity retention of 51% (Figure 4a). The charging time at 80% capacity retention, a key indicator of the fast-charging capability,^[1a] is further summarized for the $\text{PO}_2\text{-Nb}_4\text{C}_3$ and recently reported high-rate electrodes. Significantly, $\text{PO}_2\text{-Nb}_4\text{C}_3$ can be charged to 80% of the maximum capacity in 4.9 min. This charging time is much shorter than not only MXene-based electrodes for Na^+ -storage (V_2CT_x : 112.5 min,^[7a] $\text{Ti}_3\text{C}_2\text{T}_x$: 142.8 min,^[7c] Ti_2CT_x : 43.2 min^[7d]) but also well-recognized fast-charging Li^+ -storage electrodes like $\alpha\text{-MoO}_3$: 841 min,^[3a] Li_3VO_4 : 396 min,^[27] graphene: 120 min,^[28] $\text{Ti}_3\text{C}_2\text{T}_x$: 20 min,^[12a] and $\text{Li}_3\text{V}_2\text{O}_5$: 12 min^[26a] (Figure 4b and Table S2, Supporting Information). Besides, the superior rate capability of $\text{PO}_2\text{-Nb}_4\text{C}_3$ to other counterparts is also evidenced by plotting their specific capacities as a function of the charging time (Figure S23, Supporting Information). The $\text{PO}_2\text{-Nb}_4\text{C}_3$ electrode with a high mass loading of 5 mg cm^{-2} also exhibits comparable rate performance with capacity retention of 46.5% at 20 A g^{-1} , further demonstrating the excellent rate capability (Figure S24, Supporting Information).

To assess the electrochemical kinetics of the $\text{PO}_2\text{-Nb}_4\text{C}_3$ electrode, CV curves were collected at various scan rates (Figure S25, Supporting Information). Figure 4c presents the dependence of $\text{log}(i)$ versus $\text{log}(v)$ for the two pairs of redox peaks (denoted O1/R1 and O2/R2 in Figure S25, Supporting Information) of the $\text{PO}_2\text{-Nb}_4\text{C}_3$ electrode in CV curves (i refers to the peak current density, v is the scan rate). According to Equation (2), the fitting slope (b -value) of the plots is well-established as an indicator for the electrochemical kinetics.^[29] A

b -value of 0.5 identifies the diffusion-controlled process, while a b -value of 1 reveals the surface-controlled behavior. All four peaks of the $\text{PO}_2\text{-Nb}_4\text{C}_3$ electrode show close-to-1 b -values (O1: 0.97, R1: 0.84, O2: 0.93, and R2: 0.87), indicating that the Na^+ intercalation/de-intercalation processes of $\text{PO}_2\text{-Nb}_4\text{C}_3$ display a fast surface-controlled capacitive feature. Moreover, the high electrochemical kinetics of the $\text{PO}_2\text{-Nb}_4\text{C}_3$ electrode is reflected by the quantitative analysis of the CV curves (Figure 4d). Based on Equation (3),^[30] the CV curves are divided into the capacitive-controlled section (k_1v) and diffusion-controlled section ($k_2v^{1/2}$). Importantly, the capacitive contribution of the $\text{PO}_2\text{-Nb}_4\text{C}_3$ electrode accounts for 62% of the total capacity even at the minimum scan rate (0.1 mV s^{-1}). When the scan rate increases to 10 mV s^{-1} , the capacitive proportion reaches up to 94%.

$$i = av^b \quad (0.5 \leq b \leq 1) \quad (2)$$

$$i = k_1v + k_2v^{1/2} \quad (3)$$

Galvanostatic intermittent titration technique (GITT, Figure S26, Supporting Information) was used to calculate the Na^+ diffusion coefficient (D_{Na^+}) of the $\text{O-Nb}_4\text{C}_3$ and $\text{PO}_2\text{-Nb}_4\text{C}_3$ electrodes. Impressively, D_{Na^+} of $\text{PO}_2\text{-Nb}_4\text{C}_3$ (1.9×10^{-9} to $1.4 \times 10^{-8} \text{ cm}^2 \text{ s}^{-1}$),^[3a] $\text{CT-S@Ti}_3\text{C}_2$ ($7.1 \times 10^{-10} \text{ cm}^2 \text{ s}^{-1}$),^[31] Nb_2O_5 ($5.95 \times 10^{-15} \text{ cm}^2 \text{ s}^{-1}$),^[32] and $\text{P2-Na}_{2/3}\text{Ni}_{1/3}\text{Mn}_{2/3}\text{O}_2$ (10^{-10} to $10^{-9} \text{ cm}^2 \text{ s}^{-1}$).^[33] Even though the interlayer spacing of $\text{PO}_2\text{-Nb}_4\text{C}_3$ and $\text{O-Nb}_4\text{C}_3$ is close, the

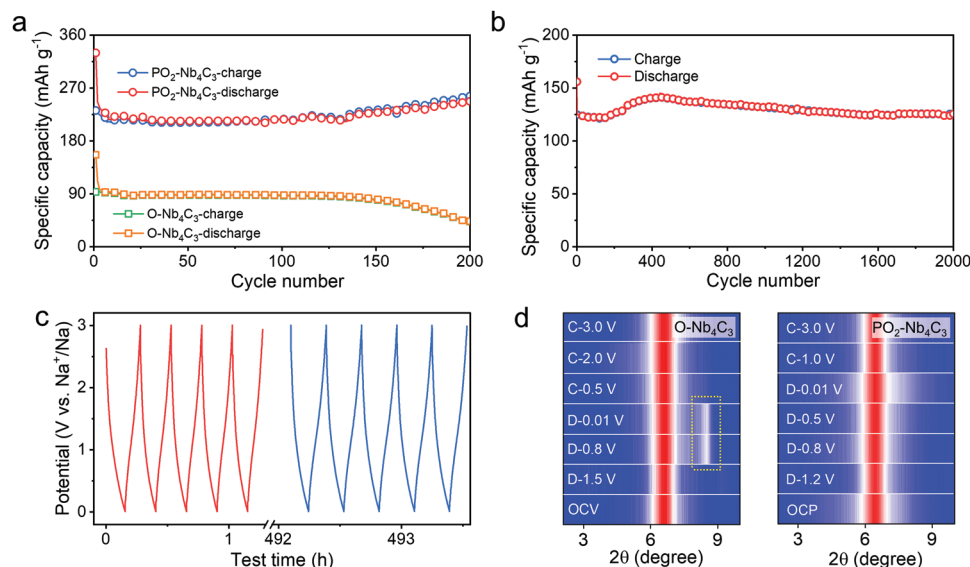


Figure 5. Cycling stability. a) Cycling performance of the O-Nb₄C₃ and PO₂-Nb₄C₃ electrodes at 0.1 A g⁻¹. b) Cycling performance of the PO₂-Nb₄C₃ electrode at 1 A g⁻¹. c) The first five and the last five cycles of the PO₂-Nb₄C₃ electrode in the cycling test at 1 A g⁻¹. d) Ex situ XRD spectra of the O-Nb₄C₃ and PO₂-Nb₄C₃ electrodes at different charge/discharge stages.

large-size PO₂-terminals do not restrict the Na⁺-diffusion compared with conventional O-terminals.

Moreover, the electrochemical impedance spectroscopy (EIS) was measured for the O-Nb₄C₃ and PO₂-Nb₄C₃ electrodes at various potentials (Figure S27, Supporting Information). Figure 4f compares the Ohmic resistance (R_s) and the charge transfer resistance (R_{ct}) of the two electrodes, which are derived by fitting the EIS results with the equivalent circuit (Figure S28, Supporting Information). As expected, the PO₂-Nb₄C₃ electrode presents both notably lower R_s and R_{ct} than O-Nb₄C₃, manifesting that PO₂-terminals enable Nb₄C₃ with improved electrical conductivity and charge transfer efficiency in comparison with O-terminals. All these results justify that PO₂-terminals can promote the charge transport of Nb₄C₃ while allowing fast Na⁺ diffusion, thus guaranteeing the PO₂-Nb₄C₃ electrode to circumvent the capacity-rate tradeoff and retain the fast-charging capability.

2.5. Improved Cycling Stability

We further demonstrate that PO₂-terminals can boost the cycling stability of Nb₄C₃ during the repeated Na⁺ intercalation/de-intercalation. In a cycling test at 0.1 A g⁻¹, the specific capacity of the O-Nb₄C₃ electrode decays rapidly to 38.1% of its initial reversible specific capacity over 200 charge/discharge cycles (Figure 5a). By contrast, the PO₂-Nb₄C₃ electrode can still maintain a high specific capacity of 256.5 mAh g⁻¹ after 200 cycles at 0.1 A g⁻¹, which is even slightly higher than the initial reversible specific capacity (231.8 mAh g⁻¹). The capacity increase of the PO₂-Nb₄C₃ electrode can be assigned to the reactivation process, which was widely identified for porous electrode materials.^[15,34] The reactivation process comes from a synergistic combination of stable SEI formation and electrolyte penetration into the porous electrode structure. Moreover,

the PO₂-Nb₄C₃ electrode can maintain 101.4% of the initial reversible specific capacity at 1 A g⁻¹ after 2000 cycles, further supporting its superior electrochemical stability (Figure 5b). Figure 5c further compares the first five and the last five GCD curves in the cycling test. No obvious change can be observed in the curve shape. Remarkably, the 3D open morphology and high-crystallinity crystal structure of PO₂-Nb₄C₃ electrode after 2000 cycles at 1 A g⁻¹ retain intact, indicating the superior structural stability of PO₂-Nb₄C₃ electrode (Figure S29, Supporting Information). Moreover, even at 10 A g⁻¹, the electrode can remain 104.9% of the initial reversible capacity after 1200 cycles (Figure S30, Supporting Information).

Ex situ XRD of both electrodes at different charge and discharge stages were carried out to understand the improved cycling stability of the PO₂-Nb₄C₃ electrode compared with the O-Nb₄C₃ electrode (Figure 5d and Figure S31, Supporting Information). Apparently, an additional XRD peak at 8.5° appears for the O-Nb₄C₃ electrode at the sodiation stages, reflecting the structural distortion of O-Nb₄C₃ induced by the Na⁺ intercalation. By contrast, the PO₂-Nb₄C₃ electrode depicts the single-phase Na⁺ intercalation/de-intercalation reaction without the presence of additional XRD peaks. The (002) peak location of PO₂-Nb₄C₃ remains the same during the charge/discharge process. Thereby, the improved cycling stability of the PO₂-Nb₄C₃ electrode can be assigned to the significant role of PO₂-terminals in buffering the internal stress of Nb₄C₃ induced by the Na⁺ accommodation and alleviating the structure distortion during the repeated Na⁺ intercalation/de-intercalation.

2.6. Na-ion Capacitors

Finally, to demonstrate the feasibility of the PO₂-Nb₄C₃ electrode in practical energy-storage applications, Na-ion capacitors (denoted PO₂-Nb₄C₃//NHPC) were assembled with the

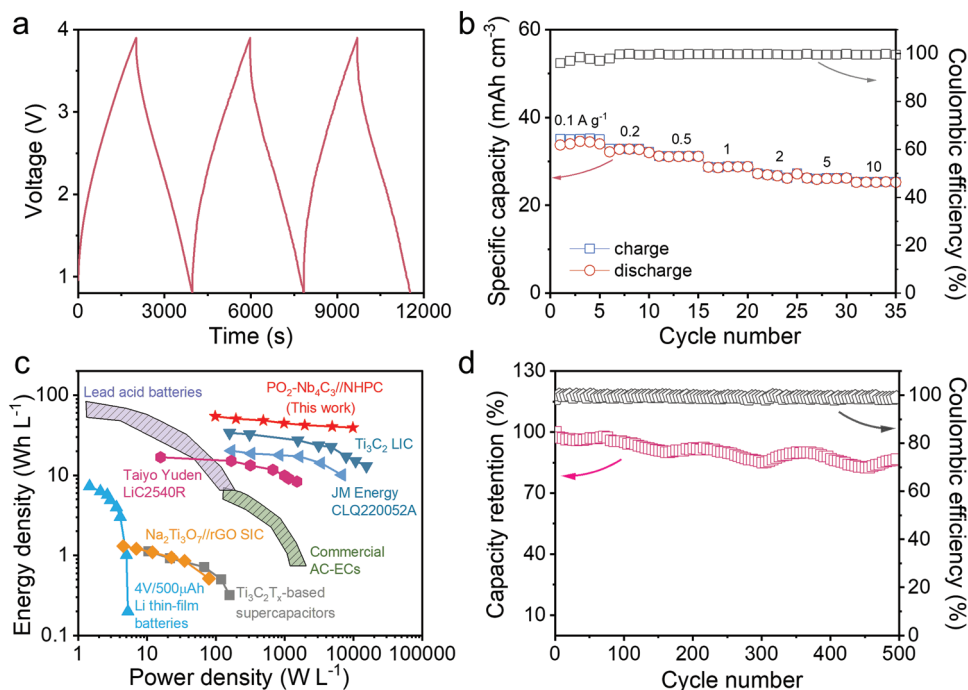


Figure 6. Full Na-ion capacitors performance. a) The initial three GCD curves at 0.1 A g^{-1} and b) device-level rate performance of the $\text{PO}_2\text{-Nb}_4\text{C}_3//\text{NHPC}$ device. c) Ragone plots of the $\text{PO}_2\text{-Nb}_4\text{C}_3//\text{NHPC}$ device in comparison with state-of-the-art energy-storage devices. d) Cycling stability of the $\text{PO}_2\text{-Nb}_4\text{C}_3//\text{NHPC}$ device tested at 2 A g^{-1} for 500 cycles with a voltage window of $0.8\text{--}3.9 \text{ V}$.

$\text{PO}_2\text{-Nb}_4\text{C}_3$ anode, brown algae-derived NHPC cathode, and 1.0 M NaPF_6 in DEGDM electrolyte. The NHPC electrode presents a capacitive Na^+ -storage behavior in a potential window of $3\text{--}4.1 \text{ V}$ versus Na^+/Na , delivering high specific capacities of 37 and 32 mAh g^{-1} at 0.05 and 5 A g^{-1} , respectively (Figure S32, Supporting Information). To enable charge balance in the cathodes and anodes of the devices, a cathode/anode mass ratio of 5 was utilized.

The electrochemical performance of the $\text{PO}_2\text{-Nb}_4\text{C}_3//\text{NHPC}$ device was evaluated by the GCD measurements from 0.1 to 10 A g^{-1} in a voltage window of $0.8\text{--}3.9 \text{ V}$ (Figure S33, Supporting Information). All GCD profiles depict approximate linear shapes, which unveils the capacitive energy-storage feature of the device. The maximum specific capacity based on the total volume of the device (illustrated in Figure S34, Supporting Information) reaches 35 mAh cm^{-3} (52 mAh g^{-1} based on active materials) at 0.1 A g^{-1} (Figure 6b). Moreover, an impressive rate capability was identified by the high capacity retention of 72% at 10 A g^{-1} (charging time: 14.5 s). The energy densities and power densities of the $\text{PO}_2\text{-Nb}_4\text{C}_3//\text{NHPC}$ device were further calculated and compared with the state-of-the-art energy-storage devices (Figure 6c and Table S3, Supporting Information). The maximum energy density of the device reached up to 54 Wh L^{-1} , remarkably surpassing those of Li thin-film batteries,^[35] $\text{Na}_2\text{Ti}_3\text{O}_7/\text{rGO}$ Na-ion capacitors,^[36] Ti_3C_2 -based Li-ion capacitors,^[12b] and supercapacitors,^[37] other commercial devices including JM energy CLQ220052A and Taiyo Yuden LIC 2540R,^[12b] and is comparable to lead-acid batteries. Moreover, the device delivered a maximum power density of 9765 W L^{-1} , which even reaches commercial active carbon-electrochemical capacitors (AC-ECs) and outperforms

some previously reported supercapacitors and hybrid ion capacitors.^[12b,36,37]

Finally, excellent cycling life was verified for the $\text{PO}_2\text{-Nb}_4\text{C}_3//\text{NHPC}$ device. After 500 charge/discharge cycles at 2 A g^{-1} , the device can maintain 86.7% of the initial capacity (Figure 6d). Even at 5 A g^{-1} , the device can retain 82.8% of the initial capacity after $10\,000$ cycles, demonstrating the long-term stability of the device (Figure S35, Supporting Information). The superior performance of the device highlights the great potential of the $\text{PO}_2\text{-Nb}_4\text{C}_3//\text{NHPC}$ device for practical energy-storage applications.

3. Conclusion

We have demonstrated constructing redox-active metaphosphate-like PO_2 -terminals as an attractive strategy to remarkably boost the Na^+ -storage ability of Nb_4C_3 MXene. Compared with conventional O-terminals, such PO_2 -terminals brought benefits to Nb_4C_3 in three aspects. First, PO_2 -terminals doubled the specific capacity of Nb_4C_3 (from 96.5 to 221.0 mAh g^{-1}) by providing additional redox sites and promoting the redox depth of Nb at the same time. Second, PO_2 -terminals improved the conductivity of the Nb_4C_3 film by an order of magnitude, while allowing Nb_4C_3 nondeclined Na^+ diffusion. This fact guaranteed the obtained $\text{PO}_2\text{-Nb}_4\text{C}_3$ to display well-retained fast-charging capability (charging time of 4.9 min at 80% capacity retention). Third, PO_2 -terminals could buffer the internal stress of Nb_4C_3 induced by the Na^+ accommodation, thus improving the cycling stability of Nb_4C_3 during the repeated Na^+ intercalation/de-intercalation. Additionally, the practical application

of the $\text{PO}_2\text{-Nb}_4\text{C}_3$ electrode was exemplified by assembling the $\text{PO}_2\text{-Nb}_4\text{C}_3//\text{NHPC}$ device with both high energy density (55 Wh L^{-1}) and large power density (9765 W L^{-1}). We hope that our results will encourage increasing efforts devoted to regulating the surface chemistry of MXenes and other 2D materials via terminal group engineering at the molecular level, which would contribute to the development of energy–power-balanced energy-storage devices.

Supporting Information

Supporting Information is available from the Wiley Online Library or from the author.

Acknowledgements

B.S., Q.L., and K.C. contributed equally to this work. This work was financially supported by European Union's Horizon 2020 research and innovation programme (GrapheneCore3 881603), M-ERA.NET and Sächsisches Staatsministerium für Wissenschaft und Kunst (HYSUCAP 100478697), and German Research Foundation (DFG) within the Cluster of Excellence, MX-OSMOPED, CRC 1415 (Grant No. 417590517), and the National Natural Science Foundation of China (Nos. 52072241 and 51772187). Z.S. was supported by Czech Science Foundation (GACR No. 19-26910X). B.S. and Q.L. were supported by the grant from China Scholarship Council. The authors acknowledge the use of the facilities in the Dresden Center for Nanoanalysis at the Technische Universität Dresden and beamtime allocation at beamlines P65 at the PETRA III synchrotron (DESY, Hamburg, Germany). The authors also thank Xia Wang, Mingchao Wang, Wei Wei, Junjie Wang, Mingming Li, and Changlin Dong for the insightful discussion.

Open access funding enabled and organized by Projekt DEAL.

Conflict of Interest

The authors declare no conflict of interest.

Data Availability Statement

Research data are not shared.

Keywords

MXenes, redox-active terminals, sodium-ion storage, hybrid-ion capacitors

Received: October 28, 2021

Revised: February 4, 2022

Published online:

- [1] a) Y. Liu, Y. Zhu, Y. Cui, *Nat. Energy* **2019**, *4*, 540; b) M. Yu, R. Dong, X. Feng, *J. Am. Chem. Soc.* **2020**, *142*, 12903.
[2] a) Y. Fang, D. Luan, X. W. D. Lou, *Adv. Mater.* **2020**, *32*, 2002976; b) H. Wang, D. Xu, R. Qiu, S. Tang, S. Li, R. Wang, B. He, Y. Gong, H. J. Fan, *Small Struct.* **2020**, *2*, 2000073.

- [3] a) M. Yu, H. Shao, G. Wang, F. Yang, C. Liang, P. Rozier, C. Z. Wang, X. Lu, P. Simon, X. Feng, *Nat. Commun.* **2020**, *11*, 1348; b) G. Wang, M. Yu, X. Feng, *Chem. Soc. Rev.* **2021**, *50*, 2388.
[4] a) B. Anasori, M. R. Lukatskaya, Y. Gogotsi, *Nat. Rev. Mater.* **2017**, *2*, 16098; b) C. J. Zhang, L. McKeon, M. P. Kremer, S. H. Park, O. Ronan, A. Seral-Ascaso, S. Barwich, C. Ó. Coileáin, N. McEvoy, H. C. Nerl, *Nat. Commun.* **2019**, *10*, 1795; c) A. VahidMohammadi, J. Rosen, Y. Gogotsi, *Science* **2021**, *372*, eabf1581.
[5] a) Z. Lin, H. Shao, K. Xu, P. L. Taberna, P. Simon, *Trends Chem.* **2020**, *2*, 654; b) S. Zheng, H. Wang, P. Das, Y. Zhang, Y. Cao, J. Ma, S. F. Liu, Z. S. Wu, *Adv. Mater.* **2021**, *33*, 2005449.
[6] A. Lipatov, A. Goad, M. J. Loes, N. S. Vorobeve, J. Abourahma, Y. Gogotsi, A. Sinitskii, *Matter* **2021**, *4*, 1413.
[7] a) S. M. Bak, R. Qiao, W. Yang, S. Lee, X. Yu, B. Anasori, H. Lee, Y. Gogotsi, X. Q. Yang, *Adv. Energy Mater.* **2017**, *7*, 1700959; b) S. Kajiyama, L. Szabova, K. Sodeyama, H. Iinuma, R. Morita, K. Gotoh, Y. Tateyama, M. Okubo, A. Yamada, *ACS Nano* **2016**, *10*, 3334; c) X. Wang, X. Shen, Y. Gao, Z. Wang, R. Yu, L. Chen, *J. Am. Chem. Soc.* **2015**, *137*, 2715; d) X. Wang, S. Kajiyama, H. Iinuma, E. Hosono, S. Oro, I. Moriguchi, M. Okubo, A. Yamada, *Nat. Commun.* **2015**, *6*, 6544; e) Y. Xie, Y. Dall'Agnese, M. Naguib, Y. Gogotsi, M. W. Barsoum, H. L. Zhuang, P. R. C. Kent, *ACS Nano* **2014**, *8*, 9606.
[8] M. R. Lukatskaya, S. Kota, Z. Lin, M. Q. Zhao, N. Shpigel, M. D. Levi, J. Halim, P.-L. Taberna, M. W. Barsoum, P. Simon, Y. Gogotsi, *Nat. Energy* **2017**, *2*, 17105.
[9] a) V. Kamysbayev, A. S. Filatov, H. Hu, X. Rui, F. Lagunas, D. Wang, R. F. Klie, D. V. Talapin, *Science* **2020**, *369*, 979; b) Y. Guo, T. Wang, Q. Yang, X. Li, H. Li, Y. Wang, T. Jiao, Z. Huang, B. Dong, W. Zhang, J. Fan, C. Zhi, *ACS Nano* **2020**, *14*, 9089; c) M. Li, X. Li, G. Qin, K. Luo, J. Lu, Y. Li, G. Liang, Z. Huang, J. Zhou, L. Hultman, P. Eklund, P. O. A. Persson, S. Du, Z. Chai, C. Zhi, Q. Huang, *ACS Nano* **2021**, *15*, 1077.
[10] Y. Xie, M. Naguib, V. N. Mochalin, M. W. Barsoum, Y. Gogotsi, X. Yu, K. W. Nam, X. Q. Yang, A. I. Kolesnikov, P. R. Kent, *J. Am. Chem. Soc.* **2014**, *136*, 6385.
[11] a) S. Xu, Y. Dall'Agnese, J. Li, Y. Gogotsi, W. Han, *Chem. - Eur. J.* **2018**, *24*, 18556; b) J. L. Hart, K. Hantanasirisakul, A. C. Lang, B. Anasori, D. Pinto, Y. Pivak, J. T. van Ommen, S. J. May, Y. Gogotsi, M. L. Taheri, *Nat. Commun.* **2019**, *10*, 522.
[12] a) Y. Li, H. Shao, Z. Lin, J. Lu, L. Liu, B. Duployer, P. O. A. Persson, P. Eklund, L. Hultman, M. Li, K. Chen, X. H. Zha, S. Du, P. Rozier, Z. Chai, E. Raymundo-Pinero, P. L. Taberna, P. Simon, Q. Huang, *Nat. Mater.* **2020**, *19*, 894; b) X. Wang, T. S. Mathis, K. Li, Z. Lin, L. Vlcek, T. Torita, N. C. Osti, C. Hatter, P. Urbankowski, A. Sarycheva, M. Tyagi, E. Mamontov, P. Simon, Y. Gogotsi, *Nat. Energy* **2019**, *4*, 241.
[13] Y. Okada, N. Keilbart, J. M. Goff, S. I. Higai, K. Shiratsuyu, I. Dabo, *MRS Adv.* **2019**, *4*, 1833.
[14] A. Lipatov, M. Alhabeb, H. Lu, S. Zhao, M. J. Loes, N. S. Vorobeve, Y. Dall'Agnese, Y. Gao, A. Gruverman, Y. Gogotsi, A. Sinitskii, *Adv. Electron. Mater.* **2020**, *6*, 1901382.
[15] S. Zhao, X. Meng, K. Zhu, F. Du, G. Chen, Y. Wei, Y. Gogotsi, Y. Gao, *Energy Storage Mater.* **2017**, *8*, 42.
[16] S. Yang, K. Zhang, A. G. Ricciardulli, P. Zhang, Z. Liao, M. R. Lohe, E. Zschech, P. W. M. Blom, W. Pisula, K. Mullen, X. Feng, *Angew. Chem., Int. Ed.* **2018**, *57*, 4677.
[17] Y. Xia, T. S. Mathis, M. Q. Zhao, B. Anasori, A. Dang, Z. Zhou, H. Cho, Y. Gogotsi, S. Yang, *Nature* **2018**, *557*, 409.
[18] J. Hu, B. Xu, C. Ouyang, S. A. Yang, Y. Yao, *J. Phys. Chem. C* **2014**, *118*, 24274.
[19] P. Nakhanev, X. Yu, S. K. Park, S. Kim, J. Y. Hong, H. J. Kim, W. Lee, J. Y. Hwang, J. E. Yang, C. Wolverton, J. Kong, M. Chhowalla, H. S. Park, *Nat. Mater.* **2019**, *18*, 156.

- [20] V. S. Mandala, D. M. Loh, S. M. Shepard, M. B. Geeson, I. V. Sergeev, D. G. Nocera, C. C. Cummins, M. Hong, *J. Am. Chem. Soc.* **2020**, *142*, 18407.
- [21] a) J. Huang, Y. Sun, Y. Zhang, G. Zou, C. Yan, S. Cong, T. Lei, X. Dai, J. Guo, R. Lu, Y. Li, J. Xiong, *Adv. Mater.* **2018**, *30*, 1705045; b) T. Zhai, L. Wan, S. Sun, Q. Chen, J. Sun, Q. Xia, H. Xia, *Adv. Mater.* **2017**, *29*, 1604167.
- [22] a) C. Zhang, H. Liu, J. He, G. Hu, H. Bao, F. Lu, L. Zhuo, J. Ren, X. Liu, J. Luo, *Chem. Commun.* **2019**, *55*, 10511; b) X. Wang, J. Shi, Z. Li, S. Zhang, H. Wu, Z. Jiang, C. Yang, C. Tian, *ACS Appl. Mater. Interfaces* **2014**, *6*, 14522.
- [23] S. Zhao, C. Chen, X. Zhao, X. Chu, F. Du, G. Chen, Y. Gogotsi, Y. Gao, Y. Dall'Agnese, *Adv. Funct. Mater.* **2020**, *30*, 2000815.
- [24] R. Ulbricht, E. Hendry, J. Shan, T. F. Heinz, M. Bonn, *Rev. Mod. Phys.* **2011**, *83*, 543.
- [25] a) X. Yao, W. Zheng, S. Osella, Z. Qiu, S. Fu, D. Schollmeyer, B. Müller, D. Beljonne, M. Bonn, H. I. Wang, *J. Am. Chem. Soc.* **2021**, *143*, 5654; b) W. Zheng, M. Bonn, H. I. Wang, *Nano Lett.* **2020**, *20*, 5807; c) G. Li, V. Natu, T. Shi, M. W. Barsoum, L. V. Titova, *ACS Appl. Energy Mater.* **2020**, *3*, 1530; d) T. L. Cocker, D. Baillie, M. Buruma, L. V. Titova, R. D. Sydora, F. Marsiglio, F. A. Hegmann, *Phys. Rev. B* **2017**, *96*, 205439.
- [26] a) H. Liu, Z. Zhu, Q. Yan, S. Yu, X. He, Y. Chen, R. Zhang, L. Ma, T. Liu, M. Li, R. Lin, Y. Chen, Y. Li, X. Xing, Y. Choi, L. Gao, H. S. Cho, K. An, J. Feng, R. Kostecki, K. Amine, T. Wu, J. Lu, H. L. Xin, S. P. Ong, P. Liu, *Nature* **2020**, *585*, 63; b) C.-C. Chen, J. Maier, *Nat. Energy* **2018**, *3*, 102.
- [27] H. Li, X. Liu, T. Zhai, D. Li, H. Zhou, *Adv. Energy Mater.* **2013**, *3*, 428.
- [28] R. Mo, F. Li, X. Tan, P. Xu, R. Tao, G. Shen, X. Lu, F. Liu, L. Shen, B. Xu, Q. Xiao, X. Wang, C. Wang, J. Li, G. Wang, Y. Lu, *Nat. Commun.* **2019**, *10*, 1474.
- [29] H. Huang, R. Xu, Y. Feng, S. Zeng, Y. Jiang, H. Wang, W. Luo, Y. Yu, *Adv. Mater.* **2020**, *32*, 1904320.
- [30] B. Chen, Y. Meng, F. Xie, F. He, C. He, K. Davey, N. Zhao, S. Z. Qiao, *Adv. Mater.* **2018**, *30*, 1804116.
- [31] J. Luo, J. Zheng, J. Nai, C. Jin, H. Yuan, O. Sheng, Y. Liu, R. Fang, W. Zhang, H. Huang, Y. Gan, Y. Xia, C. Liang, J. Zhang, W. Li, X. Tao, *Adv. Funct. Mater.* **2019**, *29*, 1808107.
- [32] L. Wang, X. Bi, S. Yang, *Adv. Mater.* **2016**, *28*, 7672.
- [33] P.-F. Wang, H.-R. Yao, X.-Y. Liu, Y.-X. Yin, J.-N. Zhang, Y. Wen, X. Yu, L. Gu, Y.-G. Guo, *Sci. Adv.* **2018**, *4*, eaar6018.
- [34] a) H. Sun, G. Xin, T. Hu, M. Yu, D. Shao, X. Sun, J. Lian, *Nat. Commun.* **2014**, *5*, 4526; b) H. Xu, W. Zhu, F. Sun, H. Qi, J. Zou, R. Laine, W. Ding, *Adv. Mater. Technol.* **2021**, *6*, 2000882; c) P. Zhang, D. Wang, Q. Zhu, N. Sun, F. Fu, B. Xu, *Nano-Micro Lett.* **2019**, *11*, 81.
- [35] D. Pech, M. Brunet, H. Durou, P. Huang, V. Mochalin, Y. Gogotsi, P. L. Taberna, P. Simon, *Nat. Nanotechnol.* **2010**, *5*, 651.
- [36] S. Dong, L. Shen, H. Li, G. Pang, H. Dou, X. Zhang, *Adv. Funct. Mater.* **2016**, *26*, 3703.
- [37] M. R. Lukatskaya, O. Mashtalir, C. E. Ren, Y. Dall'Agnese, P. Rozier, P. L. Taberna, M. Naguib, P. Simon, M. W. Barsoum, Y. Gogotsi, *Science* **2013**, *341*, 1502.